

Article

Effect of Rotational Speed on the Structural, Morphological, and Optical Properties of Biosynthesized Nickel Oxide Thin Films for Selective Solar Absorber Nanocoatings

Henok G. Gebretinsae^{1,2,3} , Meresa G. Tsegay^{1,2,3} , Giday G. Welegergs^{2,3}, Malik Maaza^{2,3} and Zebib Y. Nuru^{1,2,3,*}

¹ Department of Physics, College of Natural and Computational Science, Adigrat University, Adigrat P.O. Box 50, Ethiopia

² UNESCO—UNISA Africa Chair in Nanoscience and Nanotechnology, College of Graduate Studies, Muckleneuk Ridge, Pretoria 0001, South Africa

³ Nanosciences African Network-Materials Research Department, iThemba LABS-National Research Foundation, Cape Town 7129, South Africa

* Correspondence: zebibyenus@gmail.com

Abstract: This article presents a simple and low-cost green synthesized single-layer NiO selective solar absorber nanocoating prepared by spin coating on a Cu substrate at different rotational speeds (RS). The effects of substrate RS on the structural, morphological, chemical, and optical properties of the NiO nanocoatings were thoroughly investigated. The XRD results reveal the formation of pure diffraction peaks indexed to face-centered cubic NiO nanocoatings. SEM confirmed the uniform distribution of the NiO thin films with a nanosphere-like structure and the influence of RS variation on the formation of NiO nanostructures. EDS and XPS confirmed the presence of Ni and O in the green synthesized NiO coatings. AFM showed homogeneous nanopillar-like NiO thin films with the average surface roughness decreasing from 13.6 to 9.06 nm as the RS increased from 700 to 1300 RPM. Raman spectroscopy of the nanocoatings showed normal modes related to longitudinal optical and transverse optical phonons, and a combination of both, which implies the presence of a defect-rich or anti-ferromagnetically ordered NiO film responsible for the occurrence of more scattering peaks. UV-Vis-NIR and Fourier transform infrared spectroscopy (FTIR) were employed to characterize the optical properties of the nanocoatings. The green synthesized NiO nanocoatings deposited at 700 RPM exhibited excellent solar absorptance (α) of 0.92 and low thermal emittance (ϵ) of 0.11. The optical properties of the selective materials obtained in the present work were correlated with the non-stoichiometric nature of the spin-coated sample, multiple reflections, and interference-induced light absorption on the green synthesized surface. These results suggest that the NiO thin films prepared through this simple and environmentally benign green synthesis method can be promising candidates for efficient solar selective absorbers.

Keywords: solar energy; biosynthesis; solar absorber; spin coating; NiO



Citation: Gebretinsae, H.G.; Tsegay, M.G.; Welegergs, G.G.; Maaza, M.; Nuru, Z.Y. Effect of Rotational Speed on the Structural, Morphological, and Optical Properties of Biosynthesized Nickel Oxide Thin Films for Selective Solar Absorber Nanocoatings. *Energies* **2022**, *15*, 8960. <https://doi.org/10.3390/en15238960>

Academic Editor: Sheikh Khaleduzzaman Shah

Received: 4 November 2022

Accepted: 23 November 2022

Published: 27 November 2022

Publisher's Note: MDPI stays neutral with regard to jurisdictional claims in published maps and institutional affiliations.



Copyright: © 2022 by the authors. Licensee MDPI, Basel, Switzerland. This article is an open access article distributed under the terms and conditions of the Creative Commons Attribution (CC BY) license (<https://creativecommons.org/licenses/by/4.0/>).

1. Introduction

Nowadays, due to rapid industrial development and population growth, energy demands are constantly increasing. The use of fossil fuels, the primary energy source, has led to the emission of greenhouse gases, resulting in the depletion of the ozone layer and affecting the balance of the global environment. Solar energy, as a green and renewable resource, is abundantly available and effectively inexhaustible in most parts of the world. The use of solar energy can reduce the environmental problems caused by the consumption of fossil fuels. The conversion of solar energy to electricity or heat may be a means to help solve the energy crisis in the future, when hydrocarbon resources such as coal, gas, and oil may not satisfy the energy demand due to legislated restrictions.

Numerous methods have been introduced to convert solar radiation into different energy forms, including photovoltaics, solar cells, thermoelectric generators, solar steam generators, and solar thermal collectors. Among these, the solar thermal collector is a popular means of harvesting solar energy.

A solar thermal collector converts solar radiation into heat using the sun's energy by capturing sunlight and converting the solar radiation into heat [1–4].

In solar–thermal conversion, the main part of the solar collector is the absorber's surface, which should absorb the maximum solar radiation and convert it into heat with the minimum loss due to re-radiation in the infrared spectra [5,6]. Thus, the role of the solar absorber surface is to utilize solar radiation and to confine the energy, which suppresses heat loss to the environment. Hence, the optical and structural properties of the absorber surface are optimized to meet the key requirements of an effective solar absorber: maximum absorption of solar irradiation (0.3–2.5 μm) and minimum emission in the thermal infrared spectrum ($>2.5 \mu\text{m}$). To obtain such spectral selectivity, various designs, such as (i) intrinsic, (ii) semiconductor–metal tandems, (iii) multi-layered absorbers, (iv) metal–dielectric composite coatings, (v) textured surfaces, and (vi) selectively solar-transmitting coatings on a blackbody-like absorber, have been reported by many authors [7–14].

The absorber–reflector tandem design, which consists of a spectrally selective layer that absorbs short-wavelength solar radiation at the top and a non-selective metal substrate that has high IR reflectance at the bottom, is one of the most common methods of achieving a combination of high solar absorptance and low thermal emittance. Solar-selective absorber coatings prepared on a copper substrate are known to have low thermal emissivity, high thermal conductivity, and corrosion resistance [15].

For the preparation of such optically efficient solar absorber coatings, different fabrication techniques, such as electroplating [16], sputtering [17–20], anodization [21], chemical vapor deposition (CVD) [22–24], physical vapor deposition (PVD) [25], and electron beam evaporation [26–28] techniques, have been reported for many years.

In recent years, due to their wide range of technological applications, several researchers have studied the structural, optical, and electrochromic properties of NiO films. Aside from their outstanding performance as a semiconductor in solar cells and supercapacitors, NiO-based composites have been considered as good solar absorber coatings owing to their desirable solar selectivity of high solar absorptance and low thermal emittance. Khan et al. [29] prepared Ni/C/NiO composite thin films via the sol–gel method. They reported an absorbance of approximately 0.80 and emittance of approximately 0.11 after annealing the film at 450 °C. Similar to this, sputtered Ni–NiOx coatings deposited on an aluminum substrate with an absorptance of 0.96 and emittance of 0.047 were commercially produced as selective solar absorbers [16]. Katumba et al. [30] compared the spectral selectivity of carbon-embedded ZnO and NiO. Spectral selectivity of 0.71/0.06 and 0.84/0.04 was achieved for ZnO and NiO thin films, respectively. Roro et al. conducted additional research on C/NiO nanocomposites deposited on aluminum substrates via the sol–gel method, with a spectral selectivity of 0.85/0.12 [31].

The above-mentioned methods might be able to produce pure nanocoatings, but they have low productivity, high cytotoxicity, and are not environmentally benign. Green synthesis methods are being explored as a promising option to achieve such a goal. The toxicity reduction ability and simple synthesis process of plant leaf extracts make them a widely used resource for synthesizing various nanoparticles compared to chemical and physical synthesis methods.

This study reported the possibility of using the green synthesis method to prepare single layers of NiO nanocoatings on a Cu substrate via spin coating as a selective solar absorber. Spin coating is an ideal method because of its simplicity and cost-effectiveness in preparing thin films with good homogeneity, well-controlled thickness, crystallinity, and versatility. The effect of the rotational speed on the morphological, structural, and optical properties and performance of the prepared selective solar absorber nanocoatings is

reported. Thus far, no thorough investigation has been reported on green synthesized NiO nanocoatings as selective solar absorbers.

2. Experimental Details

2.1. Preparation of Plant Extract

Fresh leaves of *Opuntia ficus Indica* (cactus) were collected from Adigrat, Tigray, Ethiopia. The leaves were oven-dried and crushed until they formed a green paste solution. The mixture was placed in a 250 mL beaker with 100 mL of distilled water and heated at 60 °C with constant stirring for 45 min. After being filtered three times through 55 mm Labotec filter paper, the extract was kept at room temperature for 24 h.

2.2. Green Synthesis and Thin Film Deposition of NiO Nanoparticles

In this study, a concentration of 2.8 g of $\text{Ni}(\text{NO}_3)_2 \cdot 6\text{H}_2\text{O}$ precursor was added to 50 mL of the previously prepared extract solution. The mixture was then dried in a preheated oven at 100 °C for 36 h. To eliminate residual stresses and to increase the crystallinity, the dried NiO powder was annealed in a non-vacuum horizontal tube furnace at 500 °C for 2 h. The dried NiO nanopowders were stored in a tight container at room temperature, as reported in our previous work [32]. After successfully preparing the NiO nanopowder, a concentration ratio of 0.5 g of NiO nanopowder was added to 2.5 mL of distilled water. The mixture was then subjected to ultra-sonication for 20 min to produce a NiO slurry. Afterward, the solution was deposited on a Cu substrate using a vacuumed spin coater (WS-400-6NPP-Lite, Laurell Technologies, PA, USA) at different rotational speeds: 700, 900, 1100, and 1300 revolutions per minute (RPM). The Cu substrate was polished to reduce the amount of surface replication, which could influence the absorption and reflection properties of the prepared NiO nanocoatings.

Following the deposition, the samples were dried at 40 °C for 15 min, resulting in well-adhered NiO coatings on the Cu substrate.

An overview of the state of the art regarding the preparation process of green synthesized NiO nanocoatings is displayed in Figure 1a.

2.3. Possible Reaction Mechanism of Green Synthesized NiO Nanoparticles

Green synthesis of NiO nanoparticles was achieved through three chemical reactions with the solvated Ni^{2+} ions and phytochemicals from the cactus pear. These pears are rich in phytochemicals such as ascorbic acid, phenolic acid, and flavonoids [33].

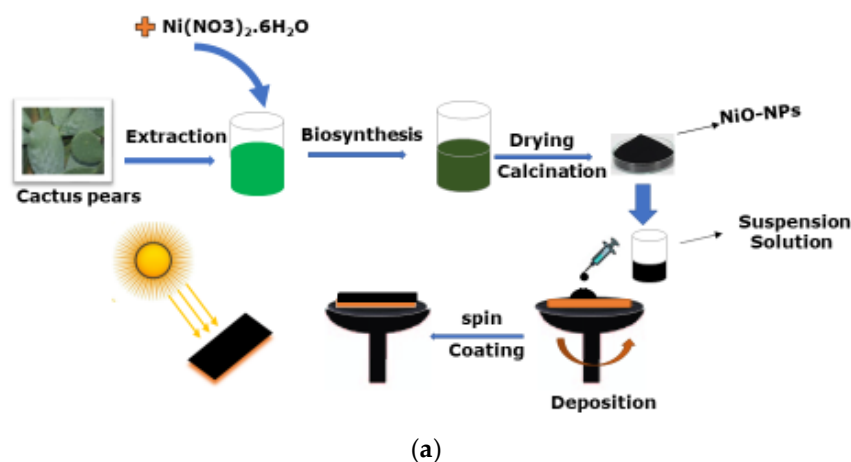


Figure 1. Cont.

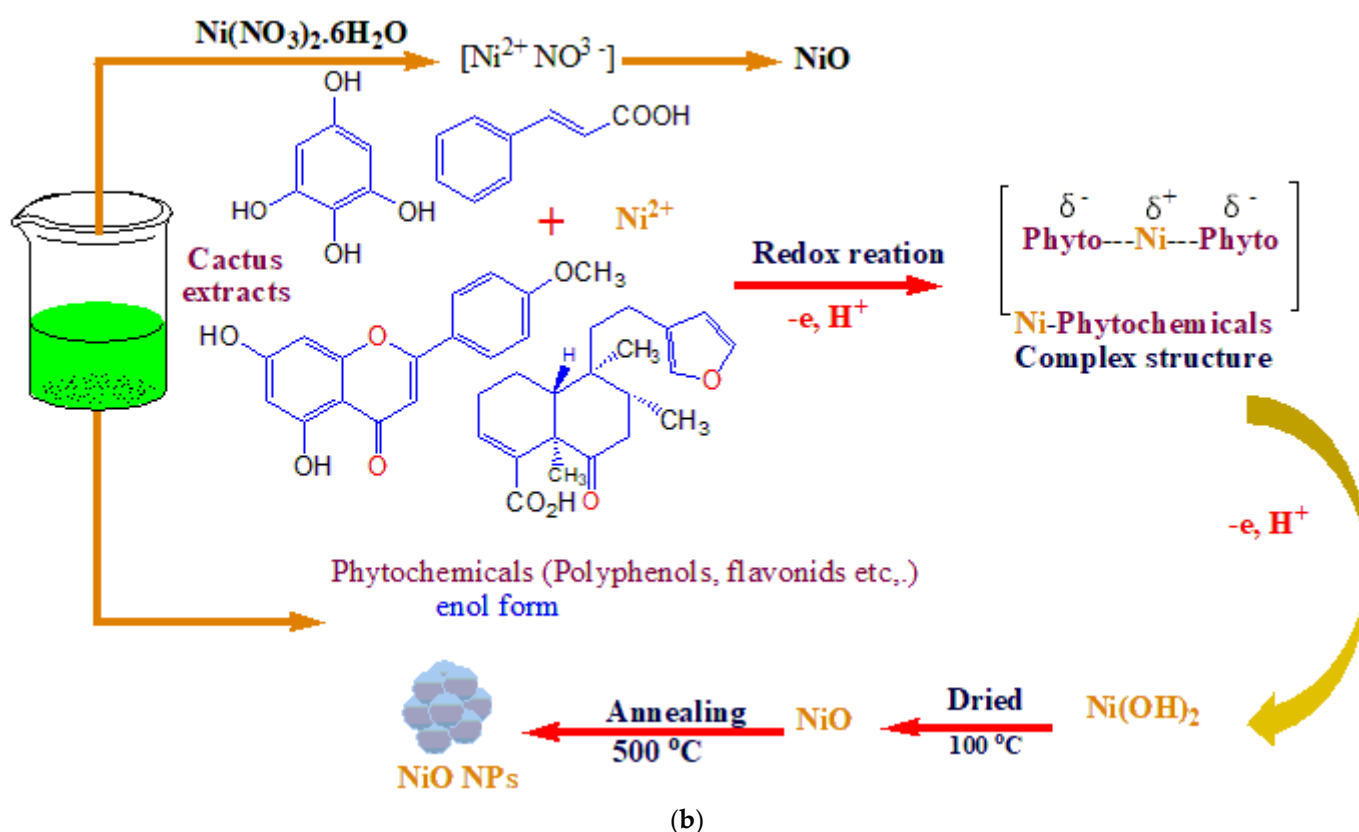


Figure 1. (a) Schematic of the green synthesis process and thin film deposition of NiO nanoparticles. (b) Possible mechanism of NiO nanoparticle formation by *Opuntia ficus Indica* leaf extract.

Opuntia ficus Indica (cactus) phytochemicals with numerous functional groups, including -C-O-, -C=C-, -C-O-H, C-N-C, and -C=O-, play a major role in the formation and stabilization of NiO nanoparticles. When $\text{Ni}(\text{NO}_3)_2 \cdot 6\text{H}_2\text{O}$ metal precursor solution is mixed with the cactus extract, it first ionizes into its respective ions (Ni^{2+}), before the bioactive compounds, such as flavonoids, phenylpropanoids, steroids, and alkaloids, reduce the metallic ions of Ni into $\text{Ni}(\text{OH})_2$. Furthermore, $\text{Ni}(\text{OH})_2$ is converted into NiO through a redox reaction after it is dried at a temperature of 100 °C. The resulting amorphous NiO is finally stabilized into NiO nanoparticles after annealing at 500 °C. The possible reaction mechanism can be summarized as in Figure 1b.

2.4. Characterization Techniques

The microstructural properties of the nanocoatings were characterized by X-ray diffraction (XRD, Model Bruker AXSD8 Advance with Cu $K\alpha$ radiation, Rigaku Cooperation, Tokyo, Japan). The morphology and elemental composition of the nanocoatings were assessed using a scanning electron microscope (SEM, Leo-Stereo Scan 440) and X-ray energy-dispersive spectroscopy (EDS), respectively.

Atomic force microscopy (AFM, Digital Instruments, Veeco Nanoscope IV Multi-Mode, Switzerland) measurement was performed to determine the surface roughness and topography of the prepared nanocoatings. The electronic structure of Ni and O was recorded by X-ray Photo Spectroscopy (XPS) (VG Scientific) using 300 W Al $K\alpha$ radiation, VG Scientific Ltd., East Grinstead, UK. Raman Spectroscopy (Jobin-Y von T64000 Raman spectrometer, USA) was used to study the changes in the chemical composition of NiO nanocoatings as a function of rotational speed (RS).

A Bruker Dektak XT profilometer was employed to determine the thickness of the green synthesized NiO nanocoatings.

The optical properties of the green synthesized NiO nanocoatings were characterized using a Cary 5000 UV–Vis–NIR spectrophotometer (Varian, Inc. model DRA-2500) in the wavelength spectrum of 0.3–2.5 μm and a Bruker Tensor 27 FT-IR spectrophotometer in the wavelength range of 4–20 μm .

The total solar absorptance (α) of the solar absorber described by integrating the spectral reflectance in the wavelength range of 0.3–2.5 μm is given by

$$\alpha = \frac{\int_{0.3}^{2.5} I_s(\lambda)(1 - R(\lambda))d\lambda}{\int_{0.3}^{2.5} I_s(\lambda)d\lambda} \quad (1)$$

where $I_s(\lambda)$ is the solar spectral irradiance at AM1.5, according to ISO standard 9845-1, and $R(\lambda)$ is the measured reflectance of the surface.

The thermal emittance (ε) is the ratio of the radiation emitted from a material surface to that of a perfect blackbody (I_b) and can be calculated from the weighted integration of the spectral reflectance with Planck's blackbody radiation distribution at 373 K [34]:

$$\varepsilon = \frac{\int_3^{30} I_b(\lambda)(1 - R(\lambda))d\lambda}{\int_3^{30} I_b(\lambda)d\lambda} \quad (2)$$

where $I_b(\lambda)$ is the solar spectral irradiance of a blackbody at a temperature T of 373 K and $R(\lambda)$ is the measured reflectance at a wavelength λ .

The effectiveness of the selective surface (η) is related to the ratio of solar absorptivity (α) and thermal emittance (ε) at temperature T:

$$\eta = \alpha/\varepsilon \quad (3)$$

3. Results and Discussion

The phase structure and composition of the samples were examined by XRD measurement. Figure 2 shows the structural characterization of green synthesized NiO films deposited on Cu substrate at RS of (a) 700, (b) 900, (c) 1100, and (d) 1300 RPM. The XRD patterns of the nanocoatings belong to the FCC structured nanocrystalline NiO (JCPDS card no. 47-1049) with unit cell parameters of $\langle a_{\text{bulk}} \rangle = \langle b_{\text{bulk}} \rangle = \langle c_{\text{bulk}} \rangle = 4.17710 \text{ \AA}$. At RS of 700 RPM, well-defined diffraction peaks of 37.2° , 43.2° , 62.8° , 75.3° , and 79.5° , corresponding to the (111), (200), (220), (311), and (222) planes of cubic NiO, respectively, were observed, as shown in Figure 2a. These sharper peaks, accompanied by a reduction in full width at half maximum (FWHM), can be correlated with an increase in the concentration and thickness of NiO films deposited at a lower RS of the copper substrate. At RS of 900 and 1100 (Figure 2b,c), a decrease in the intensity of the NiO diffraction peaks was observed. When the RS was set to 1300 RPM, the NiO diffraction peaks at 75.4° and 79.4° completely vanished, leaving only faint peaks at 37.2° and 62.9° .

The decrease in the intensity of the peaks is related to the decrease in the density of the crystals or molecules in that phase. The intensities of the reflections are determined by the distribution of the electrons in the unit cell. Planes going through areas with high electron density will reflect strongly, and planes with low electron density will give weak intensities.

As the rotational speed increases, 80–90% of the deposited solution flows to the perimeter during the deposition stage, causing a marginal decrease in the concentration and thickness of the thin films; hence, the XRD reflections are dominated by the fingerprint of the bulk copper substrate.

The lower number of nanoparticles on the surface, the less X-ray diffraction from the nanoparticles, resulting a decrease in the intensity and width of the intensity peak. This causes an in an upswing in lattice strain, a reduction in crystalline size, and an overall loss of crystallinity [35].

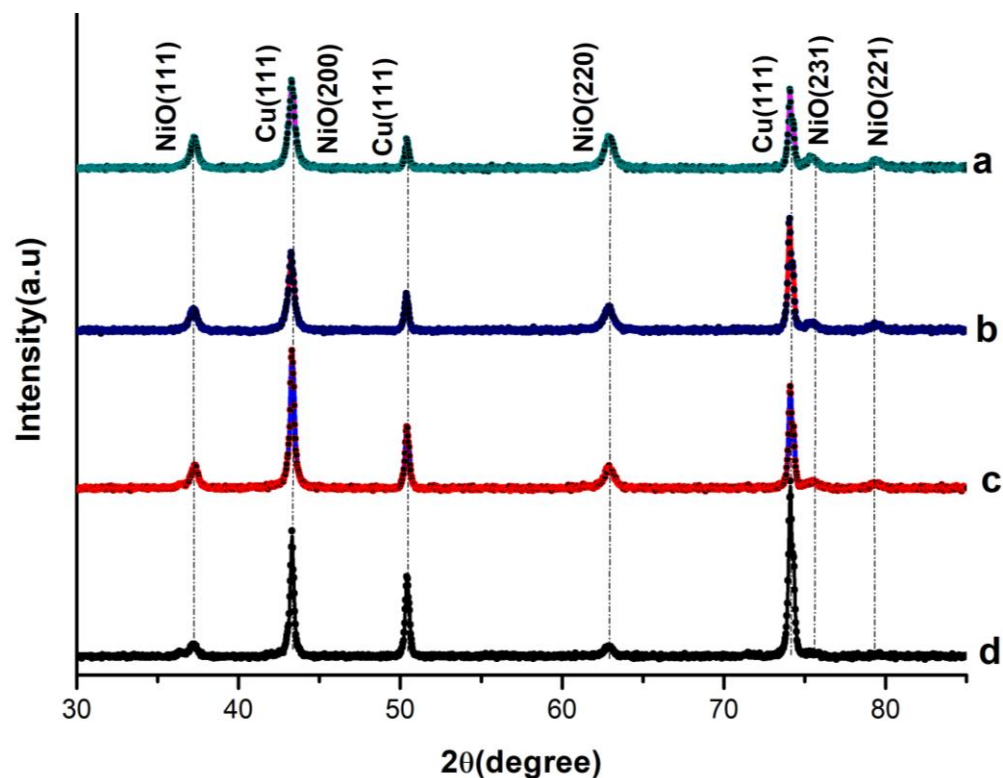


Figure 2. XRD patterns of green synthesized NiO thin films on Cu substrate prepared at rotational speeds (RS) of (a) 700 RPM, (b) 900 RPM, (c) 1100 RPM, and (d) 1300 RPM.

The appearance of four diffraction peaks at 43.2° , 50.4° , 74.1° , and 89.9° indexed to the (111), (200), (220), and (311) planes, belongs to the face-centered cubic (FCC) originating from the Cu substrate (JCPDS card no. 00-004-0836) [21]. At a diffraction angle of 2θ 43.2° , peaks from the NiO (200) film and Cu (111) substrate overlap, making it difficult to draw a conclusion on whether the peak intensity is increasing or decreasing with RS in this particular phase.

The intensity of the diffraction peaks corresponding to the copper (Cu) substrate increased with the increase in RS; this is due to the fact that, at higher RS speeds, there are more reflections from the substrate than from the film. Figure 2 also demonstrates that the positions of diffraction peaks obtained at different RS for all NiO thin films are identical, indicating the formation of a monoclinic NiO phase in all samples. The mean crystal size (D) of NiO nano-coatings was calculated from Scherrer's formula:

$$D = \frac{0.9\lambda}{FWHM \cos\theta} \quad (4)$$

where ' λ ' is the X-ray wavelength ($\lambda = 0.154056$ nm), FWHM is the full width half maximum, and ' θ ' is the Bragg angle. The inter-planar spacing $2d_{hkl}$ values of the green synthesized NiO nano-coatings can be calculated using Bragg's relation [36]:

$$2d_{hkl} \sin\theta = n\lambda \quad (5)$$

where $n = 1$ is the order of diffraction.

Taking (111) as a preferred orientation, the positions of the (111) peak, the calculated values of $d(111)$, and the lattice strain ' ϵ ' of the NiO films at different RS speeds are summarized in Table 1. The lattice constants of the NiO nano-coatings are given by $a = b = c = 4.177$ and are in good agreement with the standard values reported by JCPDS card no. 47-1049 [37].

Table 1. Crystal size, d-spacing, and lattice constant of (111) plane NiO thin film prepared at RS of (a) 700 RPM, (b) 900 RPM, (c) 1100 RPM, and (d) 1300 RPM.

	RS	2θ(111) Deg	FWHM	Crystal Size (nm)	d(111) (Å)	Strain (ε)
a	700	37.26°	0.486	18.01168	2.411	0.00652
b	900	37.28°	0.51	17.1699	2.4100	0.00684
c	1100	37.30°	0.552	15.86	2.4087	0.007399
d	1300	37.31°	0.559	13.66	2.4081	0.007491

The lattice strain of the green synthesized nanocoatings can be calculated using the following relation:

$$\varepsilon = \frac{FWHM}{4 \tan \theta} \quad (6)$$

It can be seen from the table that all the lattice strain values are positive, indicating the presence of tensile strain inside the films. The slight shift in the diffraction peaks towards a higher 2θ angle suggests that the lattice strain increased towards higher RS values, which is attributed to the change in lattice constant [37]. The trend toward reduced lattice strain at lower RS indicates that the stress has been released due to reduced lattice imperfections in the NiO films. Strain in the NiO thin film deposited at higher RS induces broadness in the diffraction peak, leading to a reduction in the crystallite size. This shift can be clearly observed in Figure 2.

Scanning electron microscopy (SEM) was employed to inspect the surface morphology of the prepared NiO samples. Figure 3a–d represent the SEM images of the green synthesized NiO thin films deposited on a copper substrate at different RS: (a) 700, (b) 900, (c) 1100, and (d) 1300 RPM. From the images, one can observe that all the prepared samples have a homogeneous and spherical-like morphology, with narrow grain boundaries, in which the rotational speed substantially impacts the size and distribution. NiO surface structures deposited at 700 and 900 RPM are densely covered and compacted when compared to thin films deposited at 1100 and 1300 RPM, demonstrating that their thickness decreases as the RS increases.

Average grain sizes were measured by Image J software. The surface of the green synthesized NiO prepared at 700 RPM is more porous, with an average grain size of ~35 nm. When we increased the RS to 900 rpm, the average grain size decreased to ~28 nm. By further raising the RS to 1100 and 1300 RPM, the grain size was decreased to 24 and 21 nm, respectively. This is because, at lower RS, the maximum number of nickel ions reaching the substrate surface results in the formation of more prominent grains and an increased number of better nucleation sites on the substrate. When we increase the RS, the concentration of Ni species will be low, making the growth rate and the nucleation process insufficient for the formation of high-quality films [38].

The surface morphology of the green synthesized NiO nanocoatings affects the solar absorptance of the coating. The spherical-like structure of the thin film deposited at low RS facilitates the trapping of radiation, resulting in the excellent absorption of solar energy at the NiO surface.

The elemental compositions of the green synthesized NiO thin films were investigated using energy-dispersive X-ray spectroscopy (EDS). The EDS spectrum shown in Figure 4a–d confirms the presence of Ni and O in the prepared samples. The elemental composition of the thin film depends on the RS of the substrate. As we increase the RS from 700 to 1300 RPM, the concentration of Ni and O species decreases, causing the copper composition to increase. This is due to the fact that as the RS increases, the film thickness decreases, allowing electrons to easily penetrate and interact with the atoms of the thin film's surface and interface on the given substrate. This results in the emergence of various signals containing information about the copper substrate [39]. The weak peaks of carbon emanated from a tape used during measurement.

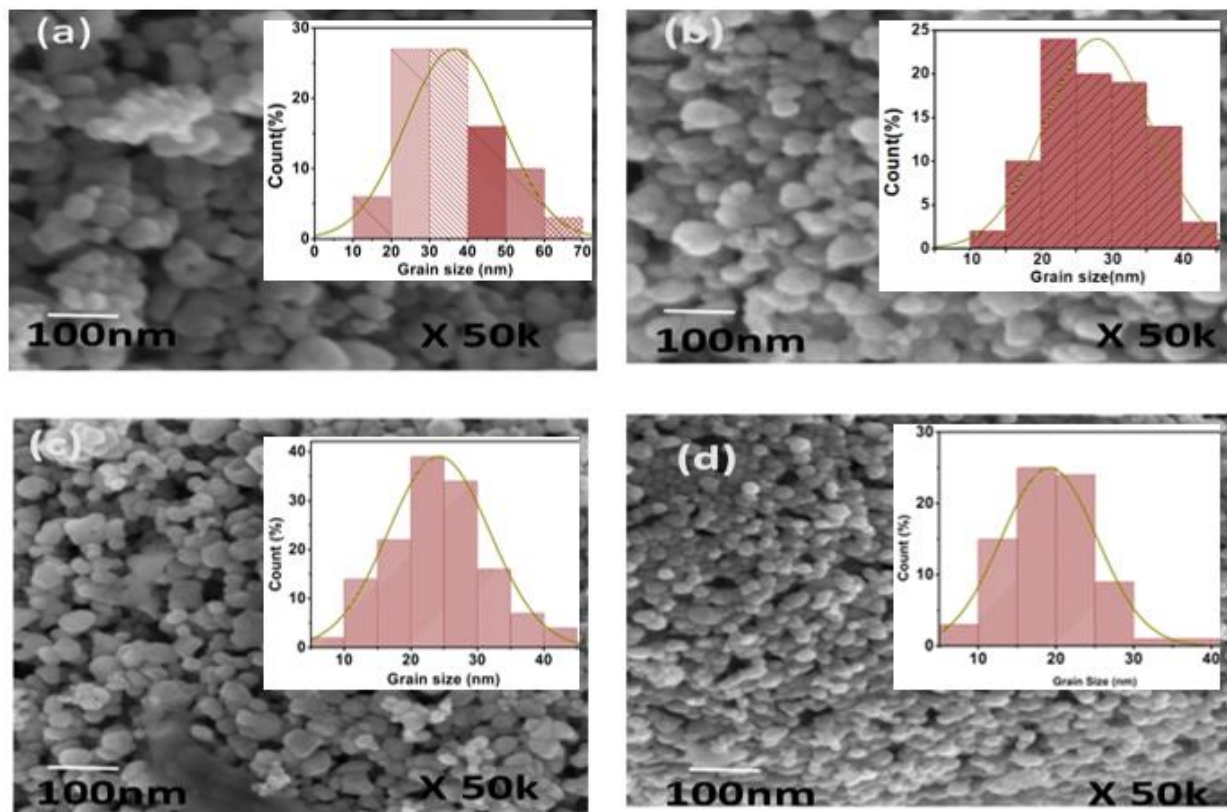


Figure 3. SEM images and size distribution histogram of the green synthesized NiO thin films on Cu substrate prepared at rotational speeds (RS) of (a) 700 RPM, (b) 900 RPM, (c) 1100 RPM, and (d) 1300 RPM.

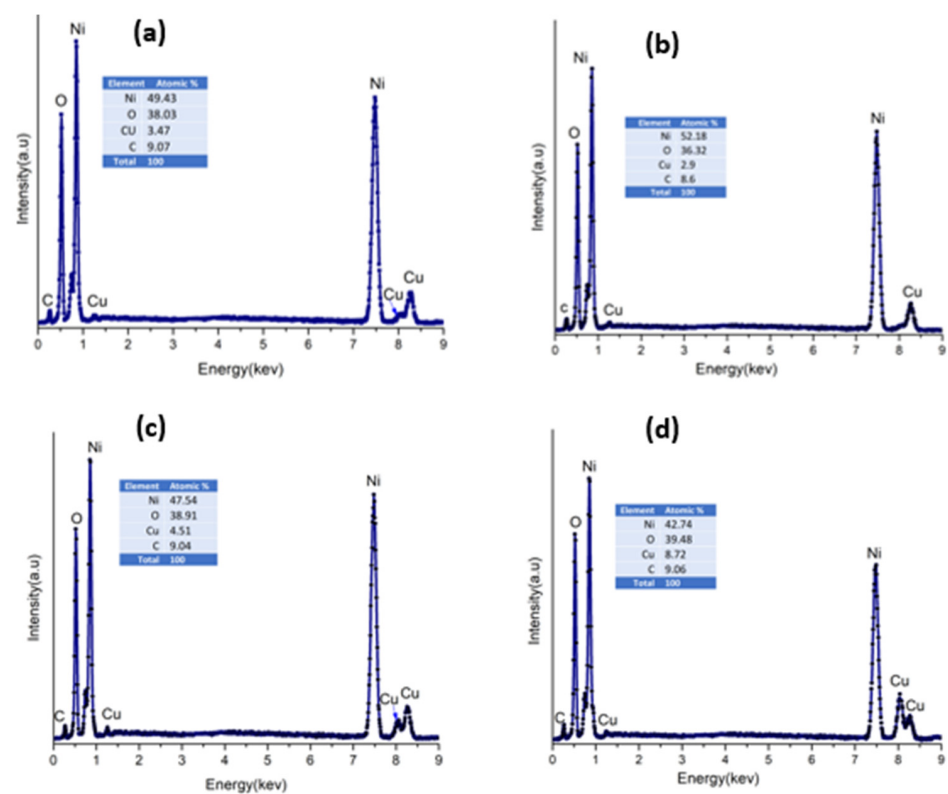


Figure 4. EDS spectrum of green synthesized NiO thin films on Cu substrate prepared at Rotational speeds (RS) of (a) 700 RPM, (b) 900 RPM, (c) 1100 RPM, and (d) 1300 RPM.

To further investigate the surface topography of the green synthesized NiO thin films, a surface roughness analysis was carried out using AFM. Figure 5 shows a 3D AFM micrograph of the green synthesized NiO at (a) 700 RPM, (b) 900 RPM, (c) 1100 RPM, and (d) at 1300 RPM on a Cu substrate. The figure depicts the formation of a nanopillar-like pattern in all the green synthesized NiO thin films as the RS changes the roughness value. The rms decreased from 13.6 to 9.06 nm as the RS was raised from 700 to 1300 RPM. The NiO films prepared at RS of 700 RPM exhibited relatively higher surface roughness, which could allow more light to be trapped due to multiple reflections within the film and thus enhanced the solar absorption. Moreover, the interface's roughness raises the index of refraction and lowers the surface reflection, which allows more light into the active selective absorber layer.

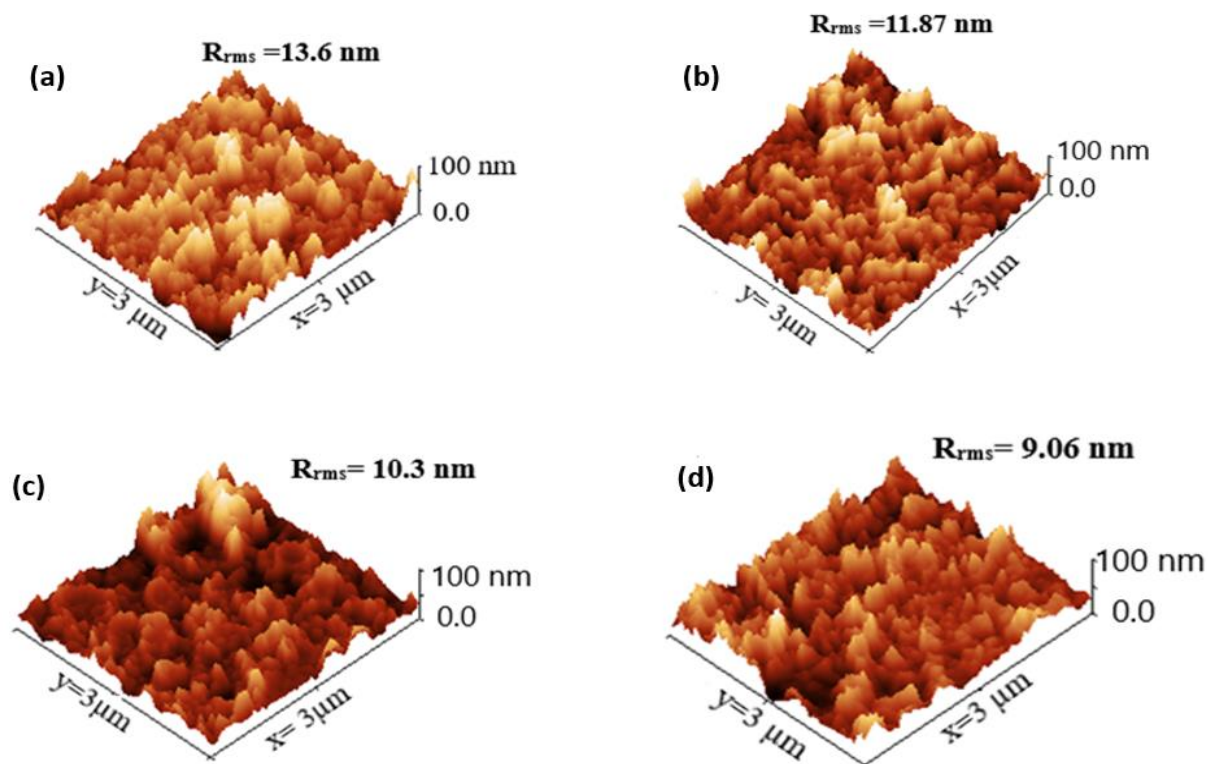


Figure 5. Three-dimensional AFM image of green synthesized NiO thin films on Cu substrate prepared at rotational speeds (RS) of (a) 700 RPM, (b) 900 RPM, (c) 1100 RPM, and (d) 1300 RPM.

The thickness of the green synthesized NiO nanocoatings was measured by a Bruker Dektak XT profilometer. The measured thickness of the films deposited at 700 RPM is 125 nm; it drops sharply to 102, 85, and 60 nm as the RS ramps up to 900, 1100, and 1300 RPM, respectively, indicating an inverse relationship between the thickness and rotational speed. Figure 6 shows the effect of RS on the thickness and surface roughness of the green synthesized NiO films. The decrease in film thickness and surface roughness with increasing RS values is consistent with the mathematical relation stating the inverse relation of thin film thickness with the square root of the angular velocity: $t \propto 1/\sqrt{\omega}$ [40].

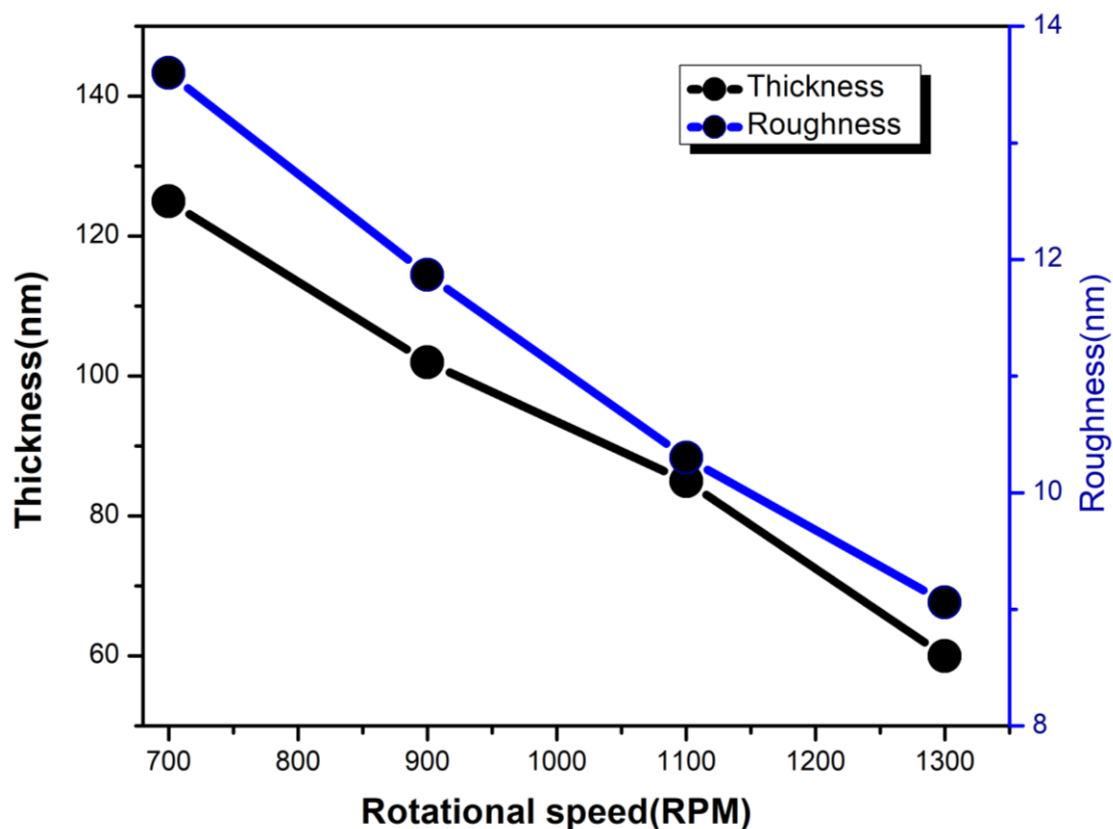


Figure 6. The variation in film thickness and surface roughness of NiO thin films as a function of rotational speed (RS).

More information on the chemical composition and electronic structure of the green synthesized NiO nanocoatings was obtained by XPS analysis through the kinetic energy analysis of both valence band and inner shell photoelectrons. Figure 7a–c show XPS spectra of green synthesized NiO nanocoatings prepared at RS of 700 RPM, 900 RPM, 1100 RPM, and 1300 RPM. The XPS survey scan was conducted using the broad survey spectra of the green synthesized NiO thin films, which were measured over a binding energy range of 0 to 1300 eV. The survey consisted of intensity peaks of Ni 3p, Ni 3s, O 1s, Ni 2p_{1/2}, Ni 2p_{3/2}, and auger electron peaks Ni LMM, O KLL, and C 1s, as shown in Figure 7a. The absence of any additional elemental peaks in the spectra implied that the deposited coatings were free of any foreign elements.

The XPS spectra were deconvoluted by Gaussian curves to determine the chemical composition of the green synthesized NiO thin films. The Ni 2p core level XPS spectra could show crucial evidence about the electronic structure of green synthesized NiO thin films deposited at various RS. The spectrum shown in Figure 7b typically exhibits well-defined 2P_{3/2} and 2P_{1/2} peaks for all the samples prepared at RS of 700 RPM, 900 RPM, 1100 RPM, and 1300 RPM and can be deconvoluted into five peaks. The 2P_{3/2} spectrum consists of the main peak at ~853 eV, a shoulder peak at ~855 eV, and a satellite peak at ~861 eV. Similarly, 2P_{1/2} shows two peaks at ~872 eV and ~879 eV, corresponding to the main and satellite peaks, respectively. These two distinct shakeup satellite peaks are the typical binding energy peaks of Ni²⁺ species, which confirms the formation of NiO NPs.

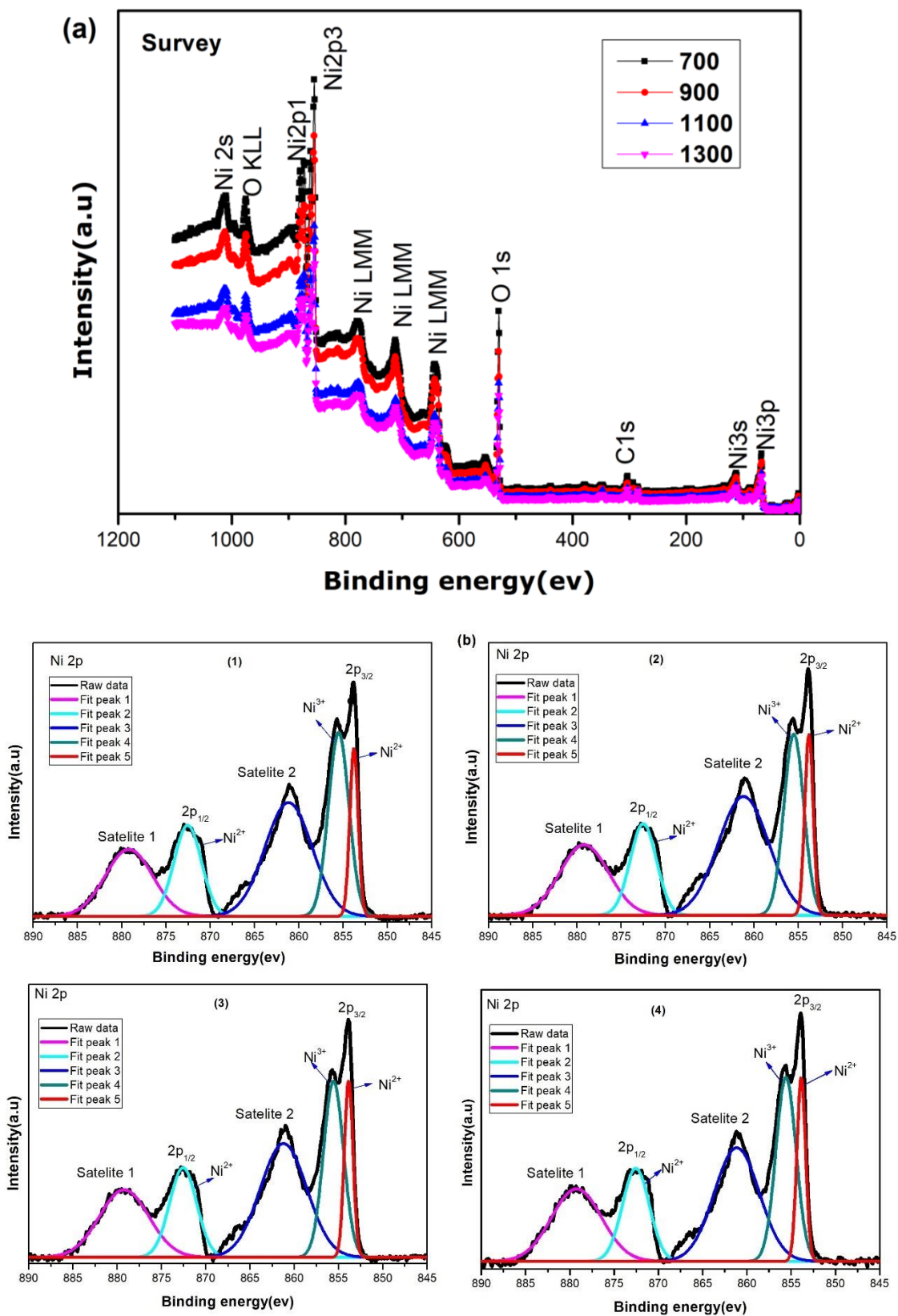


Figure 7. Cont.

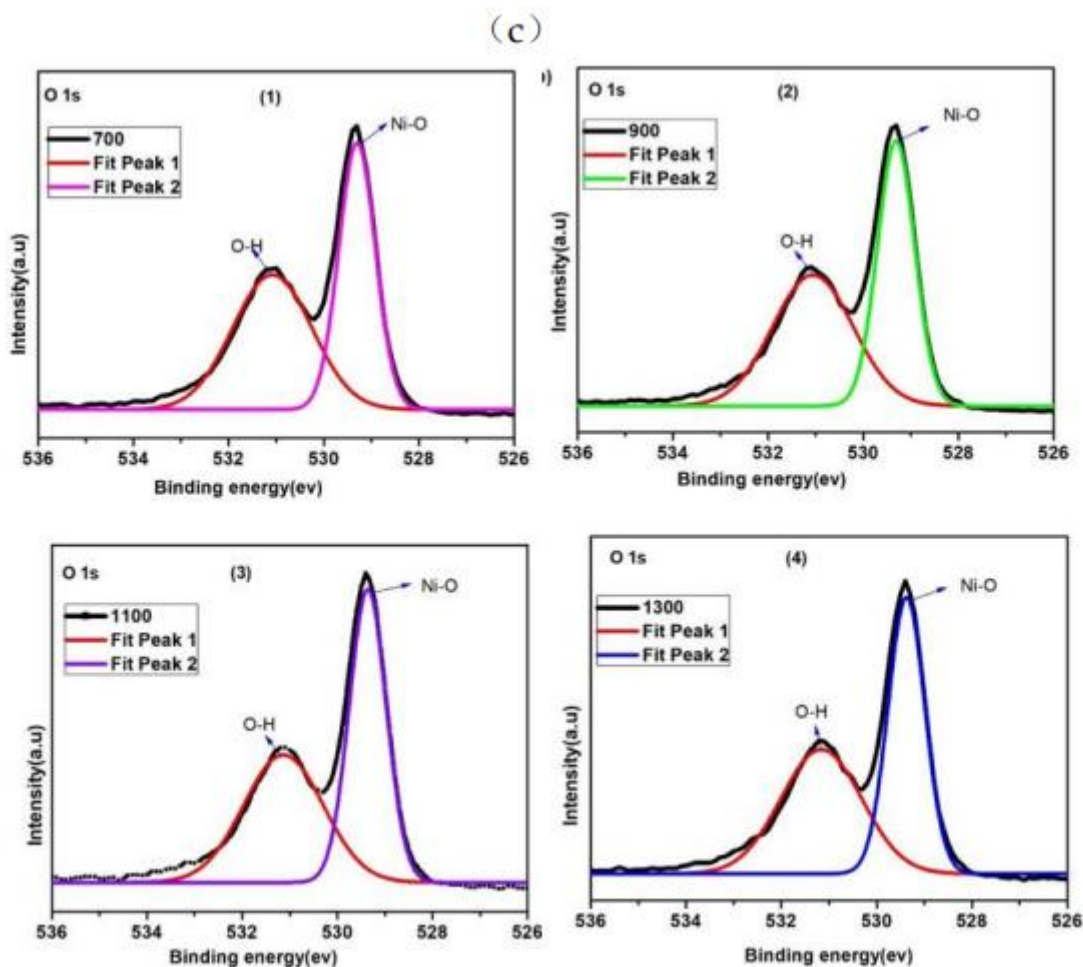


Figure 7. (a) XPS survey spectrum of green synthesized NiO thin films on Cu substrate prepared at rotational speeds (RS) of 700 RPM, 900 RPM, 1100 RPM, and 1300 RPM. (b) XPS spectra of Ni2p spectrum of green synthesized NiO thin films on Cu substrate prepared at rotational speeds (RS) of (1) 700 RPM, (2) 900 RPM, (3) 1100 RPM, and (4) 1300 RPM. (c) Typical XPS spectra of the O1s green synthesized NiO thin films on Cu substrate prepared at rotational speeds (RS) of (1) 700 RPM, (2) 900 RPM, (3) 1100 RPM, and (4) 1300 RPM.

We observed a small chemical shift to higher binding energies in the principal peaks and the satellites of Ni 2p spectra when the RS was increased from 700 to 1300 RPM. The increase in the intensity of the shoulder at ~ 855 eV of the spin-coated surface originates from the superposition of a bulk effect and Ni^{3+} species localized close to the surface. The degree of Ni 3d-O 2p hybridization, the Ni ion's valence state, its coordination symmetry with the core hole, and the defect concentration, all known to affect Ni 2p core level XPS line shapes and satellite structures, are all also responsible for this type of shift in binding energies [41,42].

The corresponding O 1s signals shown in Figure 7c are resolved into two symmetrical signals, namely peak 1 and peak 2, in all the samples by fitting with a Gaussian line shape. The lower binding energy peak at peak 1, at ~ 529 eV, corresponds to core level O^{2-} anions associated with lattice oxygen interaction in the form of Ni-O octahedral bonding of NiO [41,43]. The higher bonding energy peak at ~ 531 eV is related to the presence of excess oxygen from Ni-O-H hydroxyl bonds corresponding to metal deficiency in the green synthesized NiO thin films [44]. There is a slight shift from 529.23 to 529.38 eV in the oxidation state of Ni^{2+} as we increase the RS from 700 to 1300 RPM, which confirms the change in oxygen state and is able to enhance visible light absorption at lower RS.

Thus, at higher RS, the green synthesized NiO nanocoatings create more nickel vacancies (more Ni^{2+} ions are ionized and converted to Ni^{3+}) and oxygen interstitials, which could be attributed to the changes in the crystalline structure and defect states.

To further identify the chemical structure of the green synthesized NiO nanocoatings, Raman spectroscopy measurements were recorded in the range of $400\text{--}2000\text{ cm}^{-1}$. Figure 8 depicts room-temperature Raman spectra of the green synthesized NiO thin films prepared at RS of (a) 700 RPM, (b) 900 RPM, (c) 1100 RPM, and (d) 1300 RPM using 532 nm excitation. It is evident that the green synthesized NiO films prepared at RS of 700 RPM exhibit three Raman active peaks at $\sim 830\text{ cm}^{-1}$, $\sim 1095\text{ cm}^{-1}$, and $\sim 1372\text{ cm}^{-1}$, corresponding to two phonon (2P) transverse optical (2TO), two phonon (2P) longitudinal optical (2LO), and two-magnon (2M) bands related to the $\text{Ni}^{2+}\text{-O}^{2-}\text{-Ni}^{2+}$ super-exchange interaction of the NiO films, respectively [45,46].

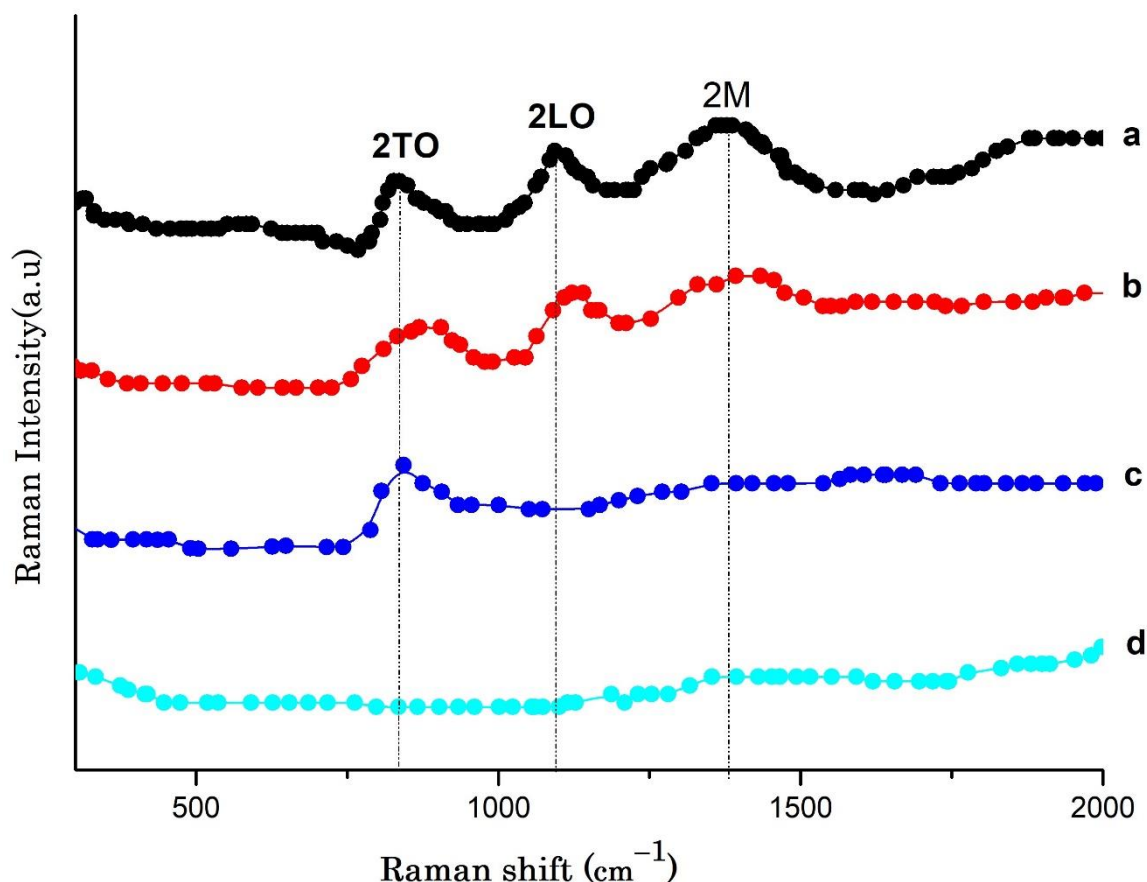


Figure 8. Raman spectra of green synthesized NiO thin films on Cu substrate prepared at rotational speeds (RS) of (a) 700 RPM, (b) 900 RPM, (c) 1100 RPM, and (d) 1300 RPM.

As the RS increased to 900 RPM, the intensity of the spectra at vibrational modes at $\sim 830\text{ cm}^{-1}$, $\sim 1095\text{ cm}^{-1}$, and $\sim 1372\text{ cm}^{-1}$ decreased. The greatest width (lower intensity) of all of these characteristic Raman peaks can be explained by the small size of the crystallites observed by XRD analysis. It was also observed that as the RS further increased to 1100 RPM, only one peak from the second-order transverse optical (2TO) phonon mode centered at $\sim 830\text{ cm}^{-1}$ was shown. The Raman peaks almost disappeared when the substrate's RS was raised to 1300 RPM. The strong Raman response at lower RS is caused by a Ni-O super-exchange mechanism, which reveals the presence of a defect-rich or antiferromagnetically ordered NiO film, responsible for the existence of more scattering peaks aside from boosting the intensity of the peaks. This is attributed to the improvement of the crystallinity of the film, as confirmed by XRD [47–49]. The deterioration of the Raman peak with an increment in RS could be in agreement with the reduced crystal sizes of the

green synthesized NiO thin films observed by XRD. This could be due to a decrease in anti-ferromagnetic spin correlations, related to an increase in Ni valence and/or interstitial O in the film. These findings are consistent with pieces of literature that have been reported [37].

Absorptance and emittance are two basic parameters used to evaluate the performance of solar absorbing materials. Figure 9a displays the UV–Vis–NIR spectral reflectance of the green synthesized NiO thin films prepared at RS of (a) 700 RPM, (b) 900 RPM, (c) 1100 RPM, and (d) 1300 RPM, measured using a UV–Vis–NIR spectrophotometer at a wavelength range of 300–2500 nm.

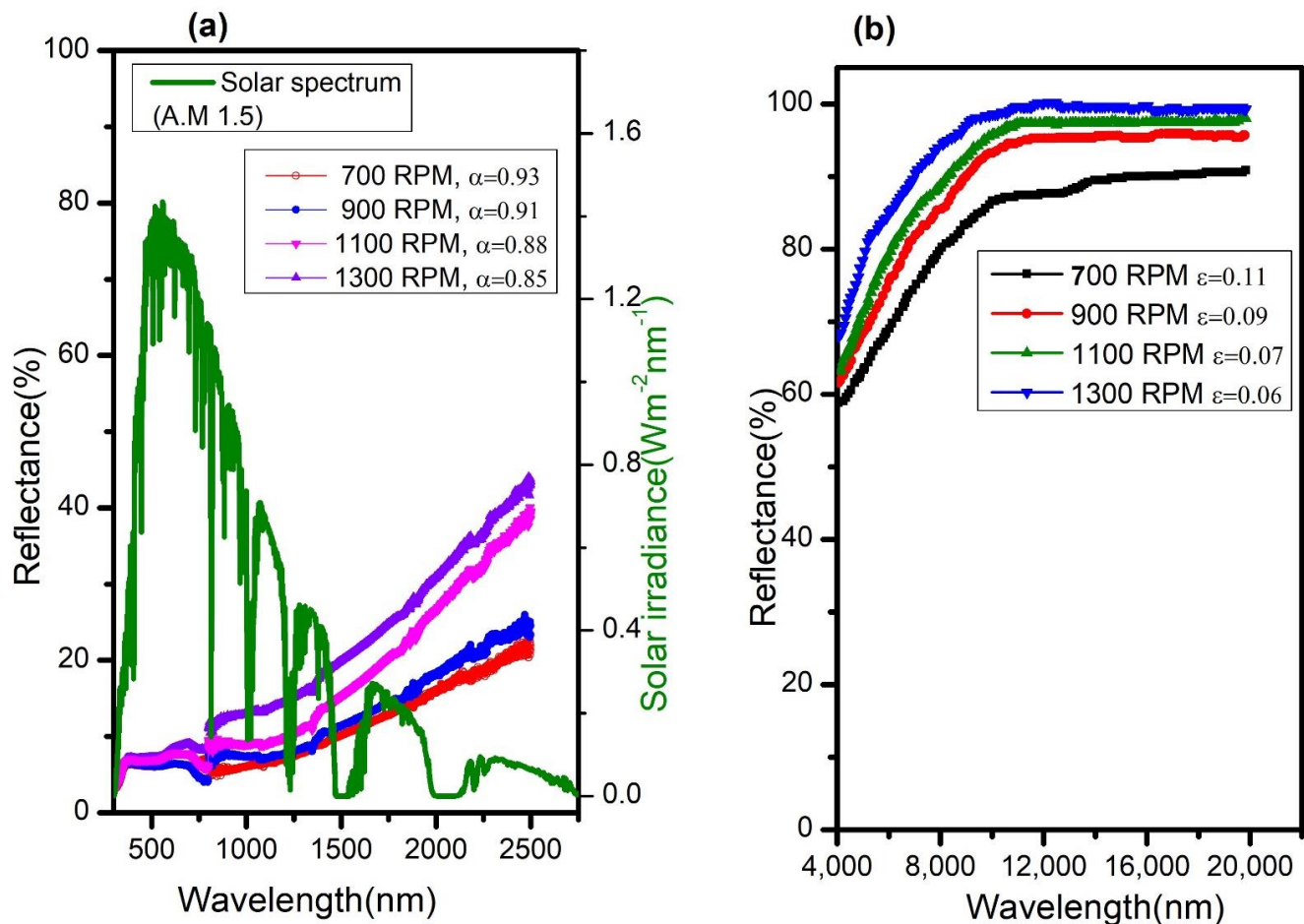


Figure 9. (a) Reflectance spectra of green synthesized NiO thin films prepared at different RS in the (a) UV–Vis–NIR region, (b) IR region.

It can be shown from Figure 9a that NiO films prepared at different RS display relatively lower reflectance in the UV–Vis spectrum and increase gradually as we shift to the near-infrared (NIR) wavelength range. This transition from lower to higher reflectance in the UV–Vis–NIR region is an indication that all the green synthesized NiO films have the ability to selectively absorb the incoming solar radiation. In addition, a curve with an interference peak was also detected in the UV wavelength range (300–390 nm) of the spectra with an average reflection of ~6% of the incident light, which indicates that more light is being absorbed in this specific range due to destructive interference effects. In contrast, the presence of an oxygen vacancy in the NiO thin films, as detected by Raman and XPS, confirmed the non-stoichiometric nature of the spin-coated sample and suggested a potential intrinsic absorption ability [50,51].

For the green synthesized NiO film prepared at 700 RPM, the reflectance somewhat increases to an average value of 7% in the range of 390–790 nm (visible spectrum), and then it steadily climbs to 25% towards the NIR region (up to 2500 nm). At 900 RPM, the surface reflectance gradually increases to ~8% in the visible region and rises to ~10% in

the longer wavelength range (701–2500 nm). Increasing the RS speed to 1100 and 1300 RPM results in a gradual increase in light reflectance to approximately ~16% and ~22%, respectively, in the NIR region, indicating that the green synthesized NiO nanocoatings prepared at different RS have high solar selectivity. The value of the solar absorptance (α) was calculated from the reflectance measurements using Equation (1). The calculated solar absorptance values decreased from 0.92 to 0.85 with the increasing RS of the green synthesized NiO nanocoatings, as shown in Table 2. This could be due to the variation in the structure, morphology, and surface roughness of the films. The green synthesized NiO films prepared at RS of 700 RPM showed a high absorptance value of $\alpha = 0.92$. This is due to multiple reflections and interference-induced light absorption on the green synthesized NiO surface, which is responsible for the significant solar absorption in the solar spectrum region [29,52–54].

Table 2. Absorptance and emittance values of the green synthesized NiO solar absorber nanocoatings prepared at different RS.

RS (RPM)	Thickness (nm)	Absorptance (α)	Emittance (ϵ) (100 °C)	Selectivity (η)
700	125	0.92	0.11	8.4
900	102	0.91	0.09	10.1
1100	85	0.88	0.07	12.6
1300	60	0.85	0.06	14.2

Similarly, when the particle size increases, reflections at the grain boundaries of the NiO thin films decrease, leading to strong depth penetration of the incident light and an increase in absorption [55]. The SEM and AFM results above offer support for this.

The spectral reflectance in the mid- and far-infrared regions of the green synthesized NiO nanocoatings was measured using FT-IR spectroscopy in the range of 4000–20,000 nm, as shown in Figure 9b. In all the samples, the percentage reflectance increased towards the far-infrared region, resulting in the desired lower thermal emittance.

Figure 9b demonstrates that the IR reflectance value of the NiO thin film prepared at 700 RPM increases from ~58% at a wavelength of ~4074 nm to ~90% at a wavelength of ~20,000 nm. For NiO films prepared at RS of 900, 1100, and 1300 RPM, the value of the IR reflectance increased to 95.5%, 98%, and 99.5%, respectively.

The solar absorptance (α), thermal emittance (ϵ), and selectivity (η) values calculated from reflectance measurements using Equations (1)–(3) are summarized in Table 2. The optical absorption (α) of the sample slightly declined from 0.92 at 700 RPM to 0.91 at 900 RPM, and ϵ changed from 0.11 to 0.09, while the coating showed an increase in spectral selectivity from 8.4 to 10.1. As the RS increased from 900 to 1100 RPM, α was reduced from 0.91 to 0.88 and ϵ declined from 0.09 to 0.07; α dropped significantly to 0.85, and ϵ also declined from 0.07 to 0.06, at an RS speed of 1300 RPM. Consequently, the spectral selectivity (α/ϵ) increased from 14.2 to 12.6.

The increase in the emittance values of these thin films at low RS is due to the high level of scattering occurring within the nano-sized grains of the NiO thin films.

At higher RS, the thickness and surface roughness of the NiO thin films decrease, allowing the incoming solar radiation to penetrate easily and reflect back from the highly metallic Cu substrate. In addition, when the dimension of the roughness of the thin film is shorter than the wavelength of the incoming solar radiation, the surface shows a flat mirror-like property, and most of the IR light will be reflected on the surface [56]. These green synthesized NiO selective solar absorbers possess excellent solar selectivity compared to NiO-based selective solar absorbers previously reported by [29,31].

4. Conclusions

In this study, a new single-layered NiO thin film as a selective solar absorber nanocoating was successfully synthesized using a green synthesis method for the first time. The green synthesized NiO was deposited onto a polished Cu substrate via spin coating at different rotational speeds (RS). The structural, morphological, compositional, and optical responses of the synthesized NiO samples showed a strong dependence on the variation in RS. XRD results revealed an improvement in the crystalline quality of the films at lower RS. SEM values confirmed the formation of uniformly distributed NiO thin films with a nanosphere-like structure. AFM showed homogeneous nanopillar-like structures with an increased average surface roughness as a function of decreasing RS. Raman spectroscopy results confirmed the presence of an anti-ferromagnetically ordered NiO film, which was responsible for the presence of more scattering peaks. Furthermore, the NiO thin film deposited at RS of 700 RPM features higher solar absorptance $\alpha = 0.92$ and a corresponding emittance value $\epsilon = 0.11$. The absorptance dropped to 0.91, 0.88, and 0.85 for the thin films prepared at 900, 1100, and 1300 RPM, respectively. The solar selectivity of the prepared thin films was observed to be greater than 8, which implies that high-performance solar-selective NiO thin films can be easily prepared by this simple and cost-effective method. Based on these analyses, it is apparent that the surface morphology and thickness play the most significant roles in determining the absorption and emissivity.

To improve the solar absorption of this sample, the application of an anti-reflection layer on top of the NiO film is underway. Nonetheless, these findings suggest that high-performance single-layered biosynthesized NiO solar absorber coatings prepared using this simple, cost-effective, and environmentally friendly method may be useful for low-temperature applications, compared to commercially available multi-layer coatings that require a complicated process and raw materials for synthesis.

Author Contributions: Methodology, M.G.T. and G.G.W.; Formal analysis, H.G.G.; Investigation, H.G.G.; Data curation, M.G.T.; Writing—original draft, H.G.G.; Writing—review & editing, Z.Y.N.; Visualization, G.G.W.; Supervision, M.M. and Z.Y.N.; Project administration, M.M. and Z.Y.N. All authors have read and agreed to the published version of the manuscript.

Funding: This research received no external funding.

Data Availability Statement: The data presented in this study are available on request from the corresponding author. The data are not publicly available due to the importance of the data for further studies.

Acknowledgments: This work was sponsored by the Future-Leader African Independent Researcher (FLAIR) fellowships from the Royal Society UK in partnership with the African Academy of Sciences (AAS), supported by the Global Challenges Research Fund (GCRF) as well as the UNESCO-UNISA Africa Chair in Nanoscience and Nanotechnology.

Conflicts of Interest: The authors declare no conflict of interest.

References

1. Tesfamichael, T. Characterization of Selective Solar Absorbers: Experimental and Theoretical Modeling. Ph.D. Thesis, Universitatis Upsaliensis, Uppsala, Sweden, 2000.
2. Zhang, K.; Hao, L.; Du, M.; Mi, J.; Wang, J.-N.; Meng, J.-P. A review on thermal stability and high temperature induced ageing mechanisms of solar absorber coatings. *Renew. Sustain. Energy Rev.* **2017**, *67*, 1282–1299. [[CrossRef](#)]
3. Dan, A.; Barshilia, H.C.; Chattopadhyay, K.; Basu, B. Solar energy absorption mediated by surface plasma polaritons in spectrally selective dielectric-metal-dielectric coatings: A critical review. *Renew. Sustain. Energy Rev.* **2017**, *79*, 1050–1077. [[CrossRef](#)]
4. Alam, T.; Balam, N.B.; Kulkarni, K.S.; Siddiqui, M.I.H.; Kapoor, N.R.; Meena, C.S.; Kumar, A.; Cozzolino, R. Performance Augmentation of the Flat Plate Solar Thermal Collector: A Review. *Energies* **2021**, *14*, 6203. [[CrossRef](#)]
5. Dias, D.; Rebouta, L.; Costa, P.; Al-Rjoub, A.; Benelmeki, M.; Tavares, C.; Barradas, N.; Alves, E.; Santilli, P.; Pischow, K. Optical and structural analysis of solar selective absorbing coatings based on AlSiOx: W cermet. *Sol. Energy* **2017**, *150*, 335–344. [[CrossRef](#)]
6. Wang, H.; Haechler, I.; Kaur, S.; Freedman, J.; Prasher, R. Spectrally selective solar absorber stable up to 900 °C for 120 h under ambient conditions. *Sol. Energy* **2018**, *174*, 305–311. [[CrossRef](#)]

7. Cao, F.; Kraemer, D.; Sun, T.; Lan, Y.; Chen, G.; Ren, Z. Enhanced Thermal Stability of W-Ni-Al₂O₃ Cermet-Based Spectrally Selective Solar Absorbers with Tungsten Infrared Reflectors. *Adv. Energy Mater.* **2015**, *5*, 1401042. [[CrossRef](#)]
8. Bilokur, M.; Gentle, A.; Arnold, M.D.; Cortie, M.B.; Smith, G.B. High Temperature Spectrally Selective Solar Absorbers Using Plasmonic AuAl₂: AlN Nanoparticle Composites. *Sol. RRL* **2017**, *1*, 1700092. [[CrossRef](#)]
9. Amri, A.; Jiang, Z.T.; Pryor, T.; Yin, C.-Y.; Djordjevic, S. Developments in the synthesis of flat plate solar selective absorber materials via sol-gel methods: A review. *Renew. Sustain. Energy Rev.* **2014**, *36*, 316–328. [[CrossRef](#)]
10. Farchado, M.; Rodríguez, J.; San Vicente, G.; Germán, N.; Morales, A. Optical parameters of a novel competitive selective absorber for low temperature solar thermal applications. *Sol. Energy Mater. Sol. Cells* **2018**, *178*, 234–239. [[CrossRef](#)]
11. Karoro, A.; Nuru, Z.; Kotsedi, L.; Bouziane, K.; Mothudi, B.M.; Maaza, M. Laser nanostructured Co nanocylinders-Al₂O₃ cermets for enhanced & flexible solar selective absorbers applications. *Appl. Surf. Sci.* **2015**, *347*, 679–684.
12. Nuru, Z.; Perez, D.; Kaviyarasu, K.; Vantomme, A.; Maaza, M. Annealing effect on the optical properties and interdiffusion of MgO/Zr/MgO multilayered selective solar absorber coatings. *Sol. Energy* **2015**, *120*, 123–130. [[CrossRef](#)]
13. Li, C.-Y.; Sari, F.N.I.; Ting, J.-M. Reactive magnetron sputter-deposited TiN_xO_y multilayered solar selective coatings. *Sol. Energy* **2019**, *181*, 178–186. [[CrossRef](#)]
14. De Maio, D.; D'Alessandro, C.; Caldarelli, A.; De Luca, D.; Di Gennaro, E.; Russo, R.; Musto, M. A selective solar absorber for unconcentrated solar thermal panels. *Energies* **2021**, *14*, 900. [[CrossRef](#)]
15. Kennedy, C.E. *Review of Mid-to High-Temperature Solar Selective Absorber Materials*; National Renewable Energy Lab.: Golden, CO, USA, 2002.
16. Wäckelgård, E.; Hultmark, G. Industrially sputtered solar absorber surface. *Sol. Energy Mater. Sol. Cells* **1998**, *54*, 165–170. [[CrossRef](#)]
17. Gelin, K. Preparation and Characterization of Sputter Deposited Spectrally Selective Solar Absorbers. Ph.D. Thesis, Universitatis Upsaliensis, Uppsala, Sweden, 2004.
18. Nuru, Z.; Kotsedi, L.; Arendse, C.; Motaung, D.; Mwakikunga, B.; Roro, K.; Maaza, M. Thermal stability of multilayered Pt-Al₂O₃ nanocoatings for high temperature CSP systems. *Vacuum* **2015**, *120*, 115–120. [[CrossRef](#)]
19. Qiu, X.-L.; Gao, X.-H.; Zhou, T.-H.; Chen, B.-H.; Lu, J.-Z.; Guo, H.-X.; Li, X.-T.; Liu, G. Structure, thermal stability and chromaticity investigation of TiB₂ based high temperature solar selective absorbing coatings. *Sol. Energy* **2019**, *181*, 88–94. [[CrossRef](#)]
20. Welegergs, G.; Gebretnisae, H.; Tsegay, M.; Nuru, Z.; Dube, S.; Maaza, M. Thickness dependent morphological, structural and optical properties of SS/CuO nanocoatings as selective solar absorber. *Infrared Phys. Technol.* **2021**, *113*, 103619. [[CrossRef](#)]
21. Kumar, S.K.; Suresh, S.; Murugesan, S.; Raj, S.P. CuO thin films made of nanofibers for solar selective absorber applications. *Sol. Energy* **2013**, *94*, 299–304. [[CrossRef](#)]
22. Randich, E.; Pettit, R. Solar selective properties and high temperature stability of CVD ZrB₂. *Sol. Energy Mater.* **1981**, *5*, 425–435. [[CrossRef](#)]
23. Seraphin, B. Chemical vapor deposition of thin semiconductor films for solar energy conversion. *Thin Solid Film.* **1976**, *39*, 87–94. [[CrossRef](#)]
24. Prasad, V.P.; Gautier, N.; Bahlawane, N. CNT nanoengineering for thermally stable selective solar absorption. *Mater. Today Commun.* **2021**, *28*, 102552. [[CrossRef](#)]
25. Selvakumar, N.; Barshilia, H.C. Review of physical vapor deposited (PVD) spectrally selective coatings for mid-and high-temperature solar thermal applications. *Sol. Energy Mater. Sol. Cells* **2012**, *98*, 1–23. [[CrossRef](#)]
26. Nuru, Z.; Arendse, C.; Muller, T.; Maaza, M. Structural and optical properties of Al_xO_y/Pt/Al_xO_y multilayer absorber. *Mater. Sci. Eng. B* **2012**, *177*, 1194–1199. [[CrossRef](#)]
27. Nuru, Z.; Msimanga, M.; Muller, T.; Arendse, C.; Mtshali, C.; Maaza, M. Microstructural, optical properties and thermal stability of MgO/Zr/MgO multilayered selective solar absorber coatings. *Sol. Energy* **2015**, *111*, 357–363. [[CrossRef](#)]
28. Kotsedi, L.; Mthunzi, P.; Nuru, Z.; Eaton, S.; Sechoghela, P.; Mongwaketsi, N.; Ramponi, R.; Maaza, M. Femtosecond laser surface structuring of molybdenum thin films. *Appl. Surf. Sci.* **2015**, *353*, 1334–1341. [[CrossRef](#)]
29. Khan, S.; Wu, Z.; Yuan, G.; Khan, M.; Song, C.; Han, G.; Liu, Y. Study of annealing effect upon the structural and solar-selective properties of C/Ni/NiO composite coatings prepared by sol-gel method. *J. Sol-Gel Sci. Technol.* **2019**, *89*, 120–127. [[CrossRef](#)]
30. Katumba, G.; Olumekor, L.; Forbes, A.; Makiwa, G.; Mwakikunga, B.; Lu, J.; Wäckelgård, E. Optical, thermal and structural characteristics of carbon nanoparticles embedded in ZnO and NiO as selective solar absorbers. *Sol. Energy Mater. Sol. Cells* **2008**, *92*, 1285–1292. [[CrossRef](#)]
31. Roro, K.T.; Tile, N.; Forbes, A. Preparation and characterization of carbon/nickel oxide nanocomposite coatings for solar absorber applications. *Appl. Surf. Sci.* **2012**, *258*, 7174–7180. [[CrossRef](#)]
32. Gebretnisae, H.; Tsegay, M.; Nuru, Z. Biosynthesis of nickel oxide (NiO) nanoparticles from cactus plant extract. *Mater. Today Proc.* **2021**, *36*, 566–570. [[CrossRef](#)]
33. Ventura-Aguilar, R.I.; Bosquez-Molina, E.; Bautista-Baños, S.; Rivera-Cabrera, F. Cactus stem (*Opuntia ficus-indica* Mill): Anatomy, physiology and chemical composition with emphasis on its biofunctional properties. *J. Sci. Food Agric.* **2017**, *97*, 5065–5073. [[CrossRef](#)]
34. Duffie, J.; Beckman, W. *Solar Thermal Engineering Processes*; A Wiley Interscience Publication: New York, NY, USA, 1980.
35. Liao, L.; Cui, Z. *Thermal Processes, in Solution Processed Metal Oxide Thin Films for Electronic Applications*; Elsevier: Amsterdam, The Netherlands, 2020; pp. 99–107.

36. Visweswaran, S.; Venkatachalapathy, R.; Haris, M.; Murugesan, R. Structural, morphological, optical and magnetic properties of sprayed NiO thin films by perfume atomizer. *Appl. Phys. A* **2020**, *126*, 524. [[CrossRef](#)]
37. Ahmed, A.A.; Hashim, M.; Rashid, M. Control of the structural, electrical and optical properties of spin coated NiO films by varying precursor molarity. *Thin Solid Film.* **2019**, *690*, 137554. [[CrossRef](#)]
38. Ganesh, V.; Haritha, L.; Anis, M.; Shkir, M.; Yahia, I.; Singh, A.; AlFaify, S. Structural, morphological, optical and third order nonlinear optical response of spin-coated NiO thin films: An effect of N doping. *Solid State Sci.* **2018**, *86*, 98–106. [[CrossRef](#)]
39. Chtouki, T.; El Mrabet, M.; Tarbi, A.; Goncharova, I.; Erguig, H. Comprehensive review of the morphological, linear and nonlinear optical characterization of spin-coated NiO thin films for optoelectronic applications. *Opt. Mater.* **2021**, *118*, 111294. [[CrossRef](#)]
40. El Sayed, A.M.; Shaban, M. Morphological, surface and optical properties of spin-coated IrOx films; influence of spin speed, annealing and (Cr, La) codoping. *Ceram. Int.* **2019**, *45*, 8460–8470. [[CrossRef](#)]
41. Scharfschwerdt, C.; Neumann, M.; Illing, G.; Freund, H. The influence of defects on the Ni 2p and O 1s XPS of NiO. *J. Phys. Condens. Matter* **1992**, *4*, 7973–7978.
42. Roberts, M.W.; Smart, R.S.C. The defect structure of nickel oxide surfaces as revealed by photoelectron spectroscopy. *Journal of the Chemical Society, Faraday Transactions 1: Physical Chemistry in Condensed Phases* **1984**, *80*, 2957–2968.
43. Biju, V. Ni 2p X-ray photoelectron spectroscopy study of nanostructured nickel oxide. *Mater. Res. Bull.* **2007**, *42*, 791–796. [[CrossRef](#)]
44. Salunkhe, P.; AV, M.A.; Kekuda, D. Investigation on tailoring physical properties of Nickel Oxide thin films grown by dc magnetron sputtering. *Mater. Res. Express* **2020**, *7*, 016427. [[CrossRef](#)]
45. Mironova-Ulmane, N.; Kuzmin, A.; Steins, I.; Grabis, J.; Sildos, I.; Pārs, M. Raman scattering in nanosized nickel oxide NiO. *J. Phys. Conf. Ser.* **2007**, *93*, 012039. [[CrossRef](#)]
46. Ascencio, F.; Bobadilla, A.; Escudero, R. Study of NiO nanoparticles, structural and magnetic characteristics. *Appl. Phys. A* **2019**, *125*, 279. [[CrossRef](#)]
47. Cazzanelli, E.; Kuzmin, A.; Mariotto, G.; Mironova-Ulmane, N. Study of vibrational and magnetic excitations in Ni_cMg_{1-c}O solid solutions by Raman spectroscopy. *J. Phys. Condens. Matter* **2003**, *15*, 2045. [[CrossRef](#)]
48. Kumar, R.; Baratto, C.; Faglia, G.; Sberveglieri, G.; Bontempi, E.; Borgese, L. Tailoring the textured surface of porous nanostructured NiO thin films for the detection of pollutant gases. *Thin Solid Film.* **2015**, *583*, 233–238. [[CrossRef](#)]
49. Jiang, D.; Qin, J.; Wang, X.; Gao, S.; Liang, Q.; Zhao, J. Optical properties of NiO thin films fabricated by electron beam evaporation. *Vacuum* **2012**, *86*, 1083–1086. [[CrossRef](#)]
50. Ivanova, T.; Harizanova, A.; Shipochka, M.; Vitanov, P. Nickel Oxide Films Deposited by Sol-Gel Method: Effect of Annealing Temperature on Structural, Optical, and Electrical Properties. *Materials* **2022**, *15*, 1742. [[CrossRef](#)]
51. Khodasevych, I.E.; Wang, L.; Mitchell, A.; Rosengarten, G. Micro- and nanostructured surfaces for selective solar absorption. *Adv. Opt. Mater.* **2015**, *3*, 852–881. [[CrossRef](#)]
52. Wang, W.; Wen, H.; Huan, X.; Shi, J.; Li, Z.; Su, J.; Wang, C. Single layer WOx films for efficient solar selective absorber. *Mater. Des.* **2020**, *186*, 108351. [[CrossRef](#)]
53. El Mahallawy, N.; Shoeib, M.; Ali, Y. Application of CuCoMnO_x coat by sol gel technique on aluminum and copper substrates for solar absorber application. *J. Coat. Technol. Res.* **2014**, *11*, 979–991. [[CrossRef](#)]
54. Kim, M.J.; Kim, H.T.; Kang, J.K.; Kim, D.H.; Lee, D.H.; Lee, S.H.; Sohn, S.H. Effects of the surface roughness on optical properties of CdS thin films. *Mol. Cryst. Liq. Cryst.* **2010**, *532*, 21/[437]–28/[444]. [[CrossRef](#)]
55. Goldschmidt, D. Determination of the absorption edge of a thin film from transmission measurements. *JOSA A* **1984**, *1*, 275–277. [[CrossRef](#)]
56. Tsegay, M.; Gebretinsae, H.; Welegergs, G.; Maaza, M.; Nuru, Z. Novel green synthesized Cr₂O₃ for selective solar absorber: Investigation of structural, morphological, chemical, and optical properties. *Sol. Energy* **2022**, *236*, 308–319. [[CrossRef](#)]